

Small-Signal Equivalent Circuit Model of Photonic Crystal Fano Laser

Aref Rasoulzadeh Zali, Mohammad Kazem Moravvej-Farshi , Senior Member, IEEE,
and Mohammad Hassan Yavari, Member, IEEE

Abstract—We develop a new small-signal equivalent circuit model for photonic crystal Fano laser based on standard linearized equations. The results are compared with those obtained by the numerical simulation approach. This novel circuit model being a cost-effective fast tool is advantageous over solving the rate equations for designing and extending the photonic crystal Fano laser. Using this circuit model, we have investigated the laser current modulation via the conventional method and via modulating the Fano mirror. The results show that the bandwidths of the amplitude modulation of the laser through-port and the frequency modulation of its cross port are both in the range of THz. It is also shown that the larger the nanocavity detuning, the greater the relaxation oscillation frequency, increasing the possibility of widening the laser bandwidth, through which the modulation efficiency may decrease. Moreover, we show that the longer the laser active region, the narrower the modulation response bandwidth. The results show that the circuit model accurately explains the photonic crystal Fano laser small-signal modulation characteristics.

Index Terms—Circuit model, Fano resonance, laser modulation, laser dynamics, photonic crystal Fano laser, small signal modulation.

I. INTRODUCTION

HIGH quality cavities and ultra-compact lasers have been realized by introducing defects in photonic crystals (PhCs), in recent years [1]–[8]. Defects in PhC membranes allow the realization of ultra-small optical cavities with high quality (Q) factors. Various types of PhC lasers such as point-defect [3], [5], line-defect [6]–[9] and nano-beam [10] lasers each with their specific advantages, have been realized. These PhC lasers are promising light sources with many applications in communication and sensing. An important feature of the PhC based cavity is that its properties can be engineered by modifying the PhC geometry to facilitate an ultra-high Q cavity and to control the output-coupling. The PhC-Fano laser (PhC-FLs) has been recently analyzed theoretically [11]–[13] and realized

Manuscript received August 20, 2018; revised February 9, 2019; accepted February 10, 2019. Date of publication February 15, 2019; date of current version March 14, 2019. The work of A. R. Zali and M. K. Moravvej-Farshi was supported by the Tarbiat Modares University under Grant #IG-39703. (Corresponding author: Mohammad Kazem Moravvej-Farshi.)

A. R. Zali and M. K. Moravvej-Farshi are with the Nano-Plasmo-Photonic Research Group, Faculty of Electrical and Computer Engineering, Tarbiat Modares University, Tehran 1411713116, Iran (e-mail: aref.rasoulzadehzali@modares.ac.ir; moravej@modares.ac.ir).

M. H. Yavari is with the Faculty of Engineering, Shahed University, Tehran 3319118651, Iran (e-mail: mh.yavari@shahed.ac.ir).

Color versions of one or more of the figures in this paper are available online at <http://ieeexplore.ieee.org>.

Digital Object Identifier 10.1109/JSTQE.2019.2899755

experimentally [14]. One of the two mirrors in this new kind of laser is provided by the Fano resonance between a discrete mode of the nanocavity and the continuum of the waveguide mode [15]–[17].

These nanolasers are of interest for many applications in integrated photonics. Accurate numerical simulation of the laser behavior is essential and computationally demanding. Nonetheless, circuit models are computationally less demanding than the device-level models are, can be used as alternative design tools. In recent years, a number of circuit models have been introduced to model the small and large signal behavior of bulk, a quantum well (QW), and quantum dot (QD) lasers [18]–[22]. These circuit models offer fast, simple, and computationally effective approaches that can best describe the laser performance from the engineers' viewpoints. So, it can be more advantageous to model the behavior of the PhC-FL by means of the electrical circuit model.

To the best of our knowledge, this paper is the first instance of describing a circuit-level implementation of the small signal behavior of a PhC-FL. In developing the circuit model, we have linearized the lasers governing differential equations. Then, the electrical circuit elements that model the laser are significantly simplified. In other words, the model is basically a set of six coupled linear electrical circuits, and by solving this set using circuit model simulator HSPICE results are predicted that are in excellent agreement with those obtained from numerical simulation of the full differential equations [11], [15] via the Runge–Kutta, and Euler methods. This newly developed circuit model provides a cost-effective fast tool for design and extends PhC-FL.

We use two modulation techniques to study the amplitude modulation (AM) and frequency modulation (FM) responses of the PhC-FL: (i) the conventional current modulation approach; (ii) the nanocavity modulation, via modulating its refractive index. Then we explain the physical origin of the large difference in modulation bandwidths obtained by the two approaches.

The paper organization is as follows. In Section II we describe the PhC-FL structure and its steady-state characteristics. In Section III the laser dynamical model is described. Accordingly, the development of the PhC-FL small signal model and the corresponding circuit model based on the linearized equations are discussed extensively. Section IV is dedicated to the analysis of the AM and FM responses of PhC-FL to the conventional current modulation and in Section V similar analyses in response to the modulation of PhC-FL nanocavity. The results

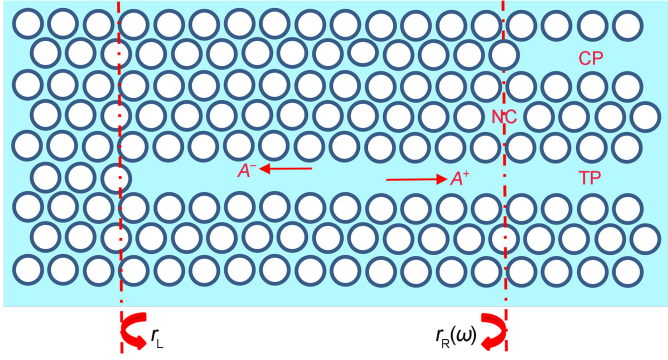


Fig. 1. Top view of the PhC-FL, wherein NC, TP, and CP represent the nanocavity, through-port, and cross-port, A^+ and A^- are the envelopes of the right and left propagating fields, and r_L and $r_R(\omega)$ represent the corresponding reflectances at the left and right mirrors. The latter is formed by Fano interference between continuum modes of the waveguide and NC discrete mode.

of the circuit model are compared with those of numerical simulations in corresponding sections. Finally, the paper is closed by the conclusion, in Section VI.

II. FANO LASER STRUCTURE AND STEADY-STATE CHARACTERISTICS

A schematic top view of the PhC-FL under study is shown in Fig. 1. It is composed of two single-ended line defect waveguides side-coupled through a point defect nanocavity (NC), devised in an airhole PhC membrane formed on a III-V semiconductor platform. The PhC bandgap effect confines the light within the plane, while in the transverse direction the light is confined by total internal reflection [23]. The destructive interference of the lower (through port) waveguide modes with the nanocavity odd mode (H_1), gives rise to a Fano resonance and forms the right mirror (r_R), known as the Fano mirror, with the effective reflectance [12], [14]:

$$r_R(\omega_s, \omega_c) = \frac{-P\gamma_c/\gamma_T}{1 + i\delta_c - (1 - i\alpha)\Gamma_c v_g g_N \Delta N_{CA}(t)/2\gamma_T} \quad (1)$$

where $\Delta N_{CA}(t) = N_{CA}(t) - N_{tr}$ represents the deviation of the instantaneous carrier density within the nanocavity, $N_{CA}(t)$, from that of the transparency, N_{tr} . $P = -1/+1$, signifies the parity of the cavity mode with respect to the mirror plane (the dots-dashes on the right side)— i.e., odd (even) mode— $\delta_c = (\omega_c - \omega_s)/\gamma_T$ is the normalized nanocavity detuning in which ω_s and ω_c represent the laser and nanocavity resonance frequencies and $\gamma_T = (\gamma_c + \gamma_i)$ represents the total decay rate in which γ_c is the nanocavity-waveguide coupling rate, and $\gamma_i = \gamma_i' + \gamma_p/2$ is the intrinsic decay rate of the nanocavity, including out of plane scattering loss, with rate γ_i' and the decay rate into the cross-port with rate γ_p (the upper waveguide). The corresponding quality factors are defined as $Q_x \equiv \omega_r/\gamma_x$ ($x = c, i, \text{ and } T$) and $Q_T^{-1} \equiv \sum_{x=c,i} Q_x^{-1}$ where ω_r is the cold resonance frequency of the nanocavity. Moreover, n_g is the group index assumed to be the same as the active medium refractive index n , c and $v_g = c/n_g$ are the light free space and group velocities, g_N , Γ_c , and α

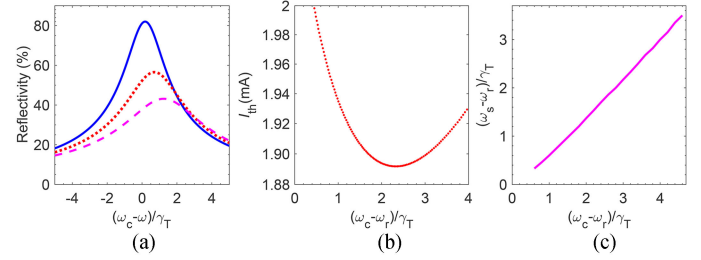


Fig. 2. (a) Fano mirror reflectance versus the normalized nanocavity detuning for three different values of the field confinement factor ($\Gamma_c = 0.1$ (solid line), 0.4 (dots), and 0.7 (dashes)). (b) and (c) the laser threshold current (I_{th}) and normalized frequency, $(\omega_s - \omega_r)/\gamma_T$, versus $(\omega_c - \omega_r)/\gamma_T$, both for $\Gamma_c = 0.4$.

represent the active region differential gain, the nanocavity field confinement factor, and Henry constant. Notice, the inclusion of N_{CA} in Eq. (1) is the consequence of the extension of the active medium over the entire membrane, specifically within the nanocavity, similar to what has been reported in [12]. In other words, the inclusion of the carrier density of the nanocavity in the equation describing the Fano mirror reflectance is because the equations governing the electromagnetic fields within the active nanocavity had to be modified, in order to provide a proper description of the laser behavior.

Furthermore, the left mirror (r_L) is formed by the reflections from the waveguide terminated end, indicated by the dots-dashes on the left side (Fig. 1). To somewhat simplify the circuit model and our calculations, we assume $r_L \approx 1$ with a broad bandwidth [11].

Beside the dependency of the Fano mirror reflectance on the detuning of the nanocavity resonant frequency from that of the laser, the third term in the denominator of Eq. (1) determines how the reflectance depends on the nanocavity absorption. Fig. 2(a) illustrates the dependency of the Fano mirror reflectance for three different values of the nanocavity field confinement factors ($\Gamma_c = 0.1, 0.4$, and 0.7). As can be seen from this figure, the larger the field confinement factor the broader the Fano mirror reflectance spectrum, with a peak shifted towards larger positive detuning.

By considering the laser oscillation and phase matching condition [11], we have calculated the PhC-FL threshold current, I_{th} , versus the nanocavity detuning, for $Q_T = 500$ and $\Gamma_c = 0.4$, (Fig. 2(b)). This figure shows that as detuning approaches its optimum value, where the Fano reflectance maximum occurs, the I_{th} decreases, first until it reaches its lowest value. Then, as detuning is increased beyond its optimum value, I_{th} increases because the phase condition is not fulfilled at the detuned frequency. Hence, the PhC-FL, in this condition, oscillates off the reflectance peak to fulfill the phase matching condition [11], [12], [14]. Furthermore, I_{th} is an asymmetric function of the nanocavity detuning $(\omega_c - \omega_r)/\gamma_T$, due to the finite value of the Henry constant (through the amplitude-phase coupling of α) [11]. The normalized laser oscillation frequency $(\omega_s - \omega_r)/\gamma_T$ versus the nanocavity detuning $(\omega_c - \omega_r)/\gamma_T$ is illustrated in Fig. 2(c), displaying a quasi-linear dependence.

III. DYNAMICAL MODEL

By combining the coupled-mode theory and the transmission line model, the dynamical model for the PhC-FL can be derived [11], [12], [14]. Dynamics of the right and left propagating field envelopes (A^+ and A^-) within the cavity can be described as [11], [12]:

$$\frac{dA^+}{dt} = \frac{1}{2} (1 - i\alpha) \Gamma v_g g_N \Delta N(t) A^+ (t) + \gamma_L \left[\frac{A^-(t)}{r_R(\omega_s, \omega_c)} - A^+(t) \right] \quad (2)$$

$$\frac{dA^-}{dt} = -\gamma_T (i\delta_c + 1) A^- - P\gamma_c A^+ (t) + \frac{1}{2} (1 - i\alpha) \Gamma_c v_g g_N \Delta N_{CA} (t) A^- (t). \quad (3)$$

where $\Delta N(t) = N(t) - N_{ss}$ represents the deviation of the instantaneous carrier density within the active region, $N(t)$, from that of the steady state, N_{ss} , $\gamma_L = v_g/2L$ is the inverse of the cavity round trip time, and Γ is the confinement factor. The third term on the right-hand side of Eq. (3) is a phenomenological absorption term that is added to account for the active nanocavity in the structure. The rate of the change in the active region carrier density can be obtained from

$$\frac{dN}{dt} = I/(eV_a) - R(N) - v_g g_N \Delta N'(t) I_P(t)/V_m \quad (4)$$

where V_a and $V_m = V_a/\Gamma$ represent the active region and the modal volumes, I represents the equivalent injection current, $R(N) = N/\tau$ is the recombination rate with τ being the effective carrier lifetime, $\Delta N'(t) = N(t) - N_{tr}$, and $I_p(t) = \sigma|A^+(t)|^2$ is the photon number in the cavity that is related to the field strength by the multiplier σ that can be determined from the steady state solutions [11]; i.e.,

$$\sigma = \frac{2\varepsilon_0 n m_g}{\hbar\omega} \frac{|r_L| + |r_R(\omega)|}{\Gamma g_N \Delta N'(t) - \alpha_i} \frac{1 - |r_R(\omega)| |r_L|}{|r_L|} \quad (5)$$

\hbar and ε_0 are the reduced plank constant and the free space permittivity. Dynamics of the nanocavity carrier density can be described as

$$\frac{dN_{CA}}{dt} = -N_{CA}(t)/\tau - \Gamma_c v_g g_N \Delta N_{CA} (t) \rho |A^-(t)|^2 / V_{CA} \quad (6)$$

where $\rho = 2\varepsilon_0 n c / \gamma_c \hbar \omega_r$ is the normalization factor similar to σ and V_{CA} is the nanocavity volume. The laser output power from the cross- and through-ports are given by:

$$P_{CP} (t) = 2\varepsilon_0 n c \gamma_p / \gamma_c |A^-(t)|^2 \quad (7)$$

$$P_{TP} (t) = 2\varepsilon_0 n c |A^+(t) - A^-(t)|^2 \quad (8)$$

The output powers from the cross- and through-ports of the PhC-FL, whose geometrical and physical parameters are given in Table I, versus the injection current, are depicted in Fig. 3 assuming $\delta_c = 0.7$ and $\Gamma_c = 0.4$. For assumed steady-state point for the Fano mirror, destructive interference between the

TABLE I
THE PHYSICAL AND GEOMETRICAL PARAMETERS OF THE PhC-FL USED IN THE SIMULATIONS [11]–[15], [17], [24]

Symbol	Quantity	Value	Unit
A_{Trans}	Transverse waveguide area	0.21	μm^2
g_N	Differential gain	5×10^{-20}	m^{-2}
L	Laser cavity length	5	μm
n	Refractive index	3.5	
N_{tr}	Transparent carrier density	10^6	μm^{-3}
Q_i	Intrinsic quality factor	5×10^4	
Q_{port}	Quality factor associated with the cross-port	1×10^4	
Q_T	Total quality factor	500	
r_L	Left facet reflectivity	1	
α	Linewidth enhancement factor	1	
α_i	Internal absorption	10	cm^{-1}
Γ	Optical confinement factor	0.5	
λ_0	Reference wavelength	1.55	μm
τ	Carrier lifetime	0.5	ns

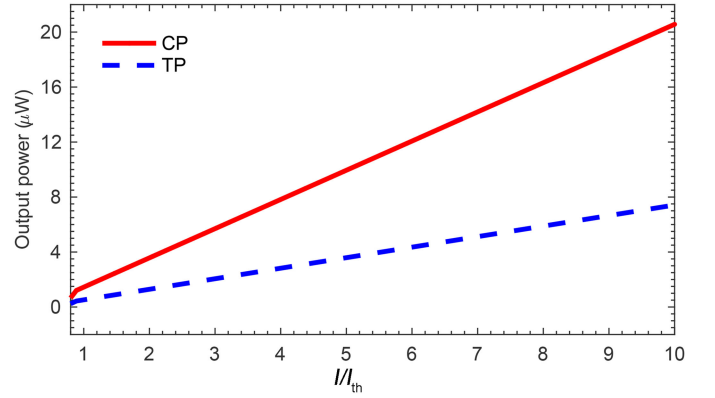


Fig. 3. Output power from the cross-port (solid line) and the through-port (dashes) of the PhC Fano laser versus the normalized injection current, with $\delta_c = 0.7$, and $\Gamma_c = 0.4$ and parameters given in Table I.

counterpropagating fields in the through-port reduces the output power compared to the cross-port. The cross-port power is proportional to the optical energy stored in the nanocavity. As a result, the power emerging from the cross-port is much larger than that of through-port. However, we shall here investigate the output properties of both ports. For numerical simulations, we have solved (1) to (6) directly, using the Runge–Kutta and Euler methods for solving the differential equations.

Using the phasorial form of the optical field envelopes $A^\pm = a^\pm \exp j\phi^\pm$, with amplitudes a^\pm and phases ϕ^\pm , the rate equations can be separated into fields' amplitude and phase derivatives. Knowing that the PhC-FL with an active nanocavity can operate in two regimes: (i) self-pulsation regime, in which a train of short pulses is generated; (ii) continuous wave (CW) regime [12]. Here, for small signal analysis, we consider the CW regime. In the presence of time-dependent small perturbations in the fields and hence the carrier densities (i.e., $a^\pm + \delta a^\pm$, $\phi^\pm + \delta \phi^\pm$, $N + \delta N$, and $N_{CA} + \delta N_{CA}$; with $\delta a^\pm \ll a^\pm$, $\delta \phi^\pm \ll \phi^\pm$, $\delta N \ll N$, and $\delta N_{CA} \ll N_{CA}$)

linearized small signal rate equations become:

$$d(\delta a^+) / dt = -\tau_{11}^{-1} \delta a^+ + \tau_{12}^{-1} \delta \phi^+ + \tau_{13}^{-1} \delta a^- + \tau_{14}^{-1} \delta \phi^- + \tau_{15}^{-1} \delta N_{CA} \quad (9)$$

$$\frac{d(\delta \phi^+)}{dt} = +\tau_{21}^{-1} \delta a^+ - \tau_{22}^{-1} \delta \phi^+ + \tau_{23}^{-1} \delta a^- + \tau_{24}^{-1} \delta \phi^- + \tau_{25}^{-1} \delta N \quad (10)$$

$$\frac{d(\delta a^-)}{dt} = +\tau_{31}^{-1} \delta a^+ + \tau_{32}^{-1} \delta \phi^+ - \tau_{33}^{-1} \delta a^- + \tau_{34}^{-1} \delta \phi^- + \tau_{35}^{-1} \delta N_{CA} \quad (11)$$

$$\frac{d(\delta \phi^-)}{dt} = \tau_{41}^{-1} \delta a^+ + \tau_{42}^{-1} \delta \phi^+ + \tau_{43}^{-1} \delta a^- - \tau_{44}^{-1} \delta \phi^- + \tau_{46}^{-1} \delta N_{CA} + \varepsilon \gamma_T \sin(2\pi f t) \quad (12)$$

$$\frac{d(\delta N)}{dt} = \frac{\Delta I}{eV_a} \sin(2\pi f t) + \tau_{51}^{-1} \delta a^+ - \tau_{55}^{-1} \delta N \quad (13)$$

$$\frac{d(\delta N)_{CA}}{dt} = \tau_{63}^{-1} \delta a^- - \tau_{66}^{-1} \delta N_{CA}. \quad (14)$$

The definitions of τ_{ij}^{-1} ($i, j = 1, 2, 3, 4, 5, 6$) in terms of the PhC-FL parameters are given in (A1)–(A6) in the Appendix. These time constants represent the rate of variation in the i -th perturbing term due to a change in the j -th term. In developing the small signal equivalent circuit model, each of the six perturbing terms can be directly related to a small signal node voltage (V_i)—i.e., $\delta a^+ = V_1(t)$, $\delta \phi^+ = V_2(t)$, $\delta a^- = V_3(t)$, $\delta \phi^- = V_4(t)$, $\delta N = V_5(t)$, and $\delta N_{CA} = V_6(t)$. Furthermore, the time constants given in (A1)–(A6) should be modeled as appropriate equivalent circuit elements. A careful inspection of (A1) and (A2) reveals that the multipliers of the forward field amplitude (δa^+) and phase ($\delta \phi^+$) of (i.e., τ_{11}^{-1} and τ_{22}^{-1}) are both directly related to the laser cavity round trip time and can be modeled as the products of two equivalent resistive (R) and capacitive (C) elements in the circuit model — i.e., $\tau_{11} \equiv R_1 C_1$ and $\tau_{22} \equiv R_2 C_2$. In other words, as the active cavity length decreases these two equivalent RC s decrease, leading to an enhanced small signal response bandwidth that is in agreement with the results reported in [11]. Similarly, the multipliers of δa^- and $\delta \phi^-$ can also be modeled as two equivalent time constants, — i.e., $\tau_{33} \equiv R_3 C_3$ and $\tau_{44} \equiv R_4 C_4$ — modeling the coupling interaction between the waveguide and nanocavity. As can be seen from (A3) and (A4), an increase in the total decay rate, γ_T , via an increase in the coupling rate between waveguide and nanocavity, γ_c , the corresponding delay time (related to $R_3 C_3$ and $R_4 C_4$) decreases, and hence, leading to an increased small signal response bandwidth [11]. Moreover, the decay rate of the charge storages in the active layer (i.e., τ_{55}^{-1}) and the nanocavity (τ_{66}^{-1}) can be modeled as $(R_5 C_5)^{-1}$ and $(R_6 C_6)^{-1}$, wherein C_5 and C_6 are the corresponding diffusion capacitances (see (A5) and A(6)). Besides, $(\Delta I / eV_a) \sin(2\pi f t) = i(t)$ and $\varepsilon \gamma_T \sin 2\pi f t = \Delta_C(t)$ on the right-hand sides of (12) and (13) are two independent AC current sources. The first source, $i(t)$, can be considered as a conventional current modulation source with amplitude $\Delta I / eV$ and frequency f , and the second source,

$\Delta_C(t)$, can be accountable for the nanocavity modulation with amplitude $\varepsilon \gamma_T$ and the same frequency, f . Moreover, the remaining time constants (τ_{ij}^{-1} with $i \neq j$) can be modeled as $C_i^{-1} G_{ij}$, noting that the products $G_{ij} V_j$ represent the dependent equivalent current sources (see A(1)–A(6) in Appendix).

Substituting the node voltages together with the equivalent circuit elements defined in (A1)–(A6), into (9)–(14) we arrive at the required differential equations for obtaining the aimed equivalent circuit model describing the PhC-FL dynamics:

$$C_1 \frac{dV_1}{dt} + \frac{V_1}{R_1} = G_{12} V_2 + G_{13} V_3 + G_{14} V_4 + G_{15} V_5 \quad (15)$$

$$C_2 \frac{dV_2}{dt} + \frac{V_2}{R_2} = G_{21} V_1 + G_{23} V_3 + G_{24} V_4 + G_{25} V_5, \quad (16)$$

$$C_3 \frac{dV_3}{dt} + \frac{V_3}{R_3} = G_{31} V_1 + G_{32} V_2 + G_{34} V_4 + G_{36} V_6, \quad (17)$$

$$C_4 \frac{dV_4}{dt} + \frac{V_4}{R_4} = G_{41} V_1 + G_{42} V_2 + G_{43} V_3 + G_{46} V_6 + \Delta_C(t), \quad (18)$$

$$C_5 \frac{dV_5}{dt} + \frac{V_5}{R_5} = G_{51} V_1 + i(t), \quad (19)$$

$$C_6 \frac{dV_6}{dt} + \frac{V_6}{R_6} = G_{63} V_3 \quad (20)$$

Equations (15)–(20) describe the dynamics of the equivalent circuit models, illustrated in Fig. 4. The proposed circuit model is based on the Kirchhoff circuit law. We will simulate this set of six coupled linear equations via HSPICE circuit simulator and compare these results with those obtained from simulation of Eqs. (1)–(6) via the Runge–Kutta, and Euler methods.

IV. CURRENT MODULATION

In this section, we modulate the PhC FL via current modulation. In doing so, we first use the new circuit model represented by Eqs. (15)–(20) and Fig. 4 and predict the modulation properties of the PhC-FL. Then, for the sake of comparison, we solve the rate equations (1)–(6) numerically, using the Runge–Kutta, and Euler methods. The power modulation index of the through or cross-port, for any given injection current and modulation amplitude, is defined as the ratio of the maximum excursion of the optical power to the average power emerging from the corresponding port. Moreover, the frequency response or FM amplitude of each field is defined as the maximum excursion of the instantaneous optical frequency, $\nu(t) = -\partial_t \phi(t)$ of that field.

Considering a fixed modulation amplitude, $\Delta I = 95 \mu A$, and three different (static) injection currents of $I/I_{th} = 2, 6$, and 10 , we have simulated the power modulation indices of the through and cross-ports of the PhC-FL versus frequency. The simulations were performed using the circuit and numerical models. The solid lines ($2I_{th}$), dashes ($6I_{th}$), and dots-dashes ($10I_{th}$) in Fig. 5(a) and 5(b) represent the results of the circuit models, compared with the asterisk representing the results of numerical simulations. A similar comparison for the FM amplitudes of the cross port versus frequency is illustrated in Fig. 5(c). The

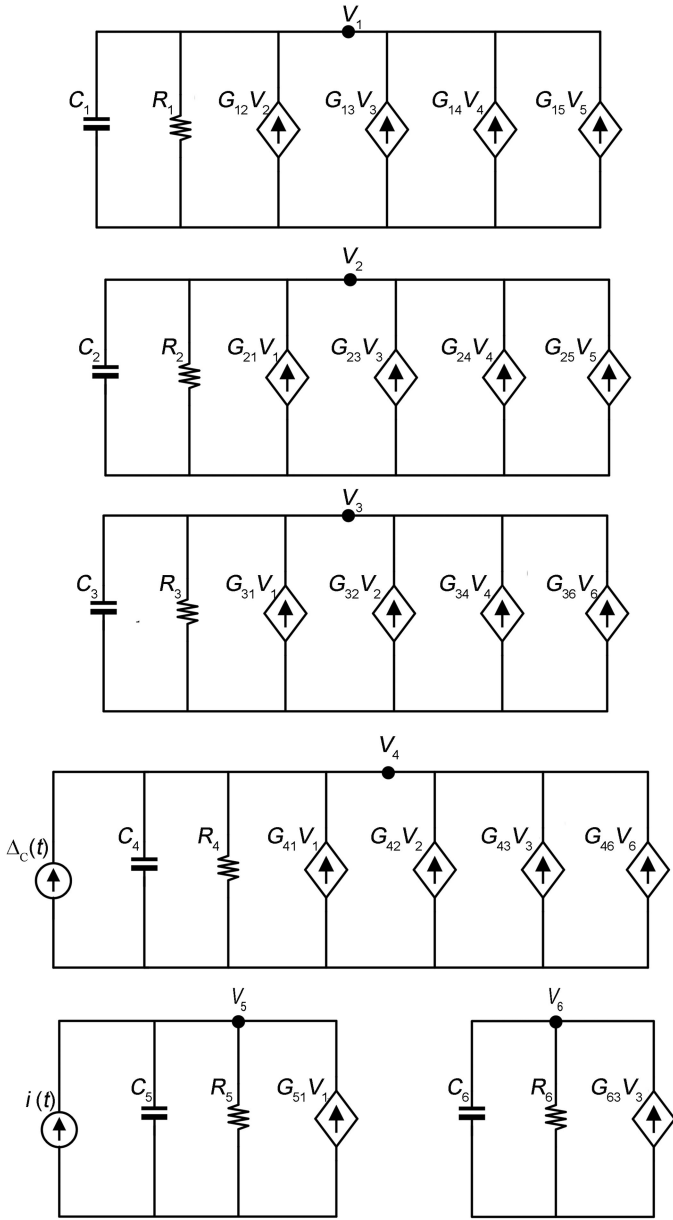


Fig. 4. Small-signal equivalent circuit model of the PhC-FL with active nanocavity.

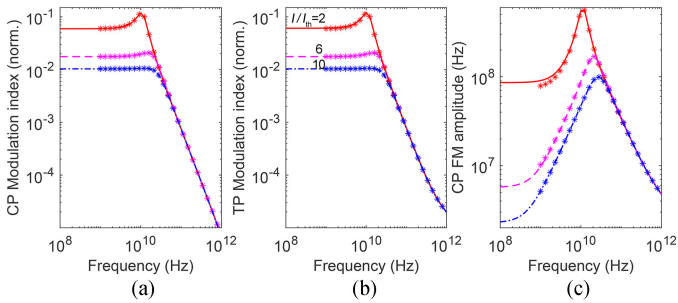


Fig. 5. Frequency response of the power modulation index for the PhC-FL (a) cross-port, (b) through-port (b); (c) FM modulation amplitude of the cross-port field (A^-), for three different injection currents: $III_{th} = 2$ (solid lines), 6 (dashes), and 10 (dots-dashes). $\Delta I = 95 \mu$, $\Gamma_c = 0.4$, and $\delta_c = 0.7$. Lines depict the circuit model simulation results and asterisk represent the data obtained via numerical approach.

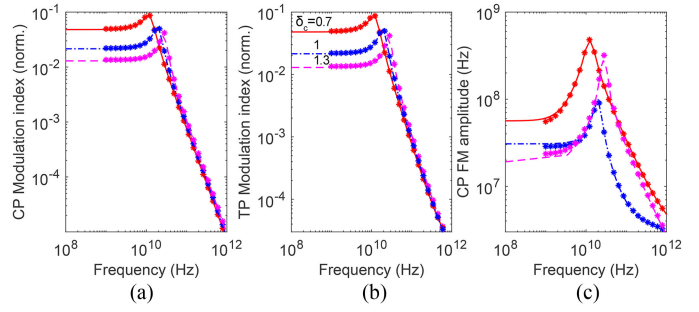


Fig. 6. Frequency response of the power modulation index for the PhC-FL (a) cross-port, (b) through-port (b); (c) FM modulation amplitude of the cross-port field (A^-), for different nanocavity detuning values of $\delta_c = 0.7$ (solid line), 1 (dashes), and 1.3 (dots-dashes). $I_p = 2.05 \times 10^4$, $I = 5 I_{th}$, $\epsilon = 0.07$, and $\Gamma_c = 0.4$. Lines depict the model simulation results and asterisk represent the data obtained via numerical approach.

comparisons show excellent agreements between the numerical and circuit models. As can be seen from Fig. 5(a) and 5(b) the larger the injection current or the smaller the ΔIII ratio, the smaller the low frequency component of the modulation indices. Moreover, the larger the injection current, the larger the relaxation oscillation frequency and the 3-dB bandwidth of PhC-FL, similar to the conventional FP laser. For example, the relaxation oscillation frequencies corresponding to the injection currents $III_{th} = 2, 6, \text{ and } 10$ are $f_R = 10 \text{ GHz}, 18 \text{ GHz}, \text{ and } 22 \text{ GHz}$, respectively. Fig. 5 also reveals that for frequencies lower than relaxation oscillation frequency ($f < f_R$) the modulation indices are almost independent of the frequency, while the corresponding FM amplitudes increase with a large and positive slope. These behavior for the modulation indices and FM amplitudes of the PhC-FL in the low-frequency region are similar to the those of conventional FP lasers [25].

Next, we consider the photon number to be constant, $I_p = 2.05 \times 10^4$, and simulate PhC-FL modulation responses for three different detunings, $\delta_c = 0.7, 1, \text{ and } 1.3$, using both models. Fig. 6 illustrates the comparisons, similar to those depicted in Fig. 5. As can be seen from Fig. 6, for the same intracavity photon number, the larger the Fano laser nanocavity detuning, the larger the relaxation oscillation frequency and the 3-dB bandwidth. For example, the relaxation oscillation frequencies corresponding to the detunings, $\delta_c = 0.7, 1, \text{ and } 1.3$, are $f_R = 13 \text{ GHz}$ (solid lines), 21 GHz (dashes), and 28 GHz (dots-dashes), respectively. In fact, the larger the nanocavity detuning, the smaller the Fano mirror reflectivity and hence the shorter the photon lifetime and the higher the relaxation oscillation frequency [25]. Nonetheless, one should notice that increasing the nanocavity detuning greatly reduces the modulation efficiency.

V. NANOCAVITY MODULATION

Similar to what we have demonstrated in Section IV, in this section too, we first use the newly developed circuit model to investigate the frequency responses of the PhC-FL through- and cross-ports to the modulation of the nanocavity refractive index that can modulate the nanocavity resonance frequency and detuning. Then, we compare these new results with the similar

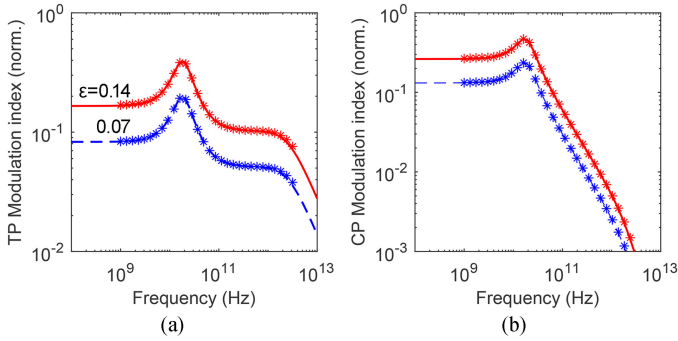


Fig. 7. The intensity modulation index of the (a) through-port and (b) cross-port versus the nanocavity modulation frequency, for $\varepsilon = 0.07$ (dashes) and 0.14 (solid lines) obtained via circuit model simulations. Asterisk represents the results of numerical simulations.

data obtained by solving the rate equations numerically, using the Runge–Kutta, and Euler methods. The nanocavity modulation may be fulfilled by (i) using a near-field probe to modify the nanocavity resonance frequency [26]; (ii) applying voltage to the electrode that is placed near the nanocavity [27]; and (iii) using optical nonlinearities [24], [28]. By modulating the Fano mirror resonance frequency, the amplitude and phase of the laser will both be modulated simultaneously, since the mirror reflectivity and phase both depend on the nanocavity resonance frequency. In other words, the Fano mirror modulation results in amplitude and phase modulation at the same time. Fig. 7 illustrates the modulation indices of the (a) through-port and (b) cross-port powers versus the modulation frequency for an injection current of $I = 5 I_{th}$ and modulation amplitudes of $\varepsilon = 0.14$ (solid lines) and $\varepsilon = 0.07$ (dashes), simulated by the circuit model that are compared with results of numerical simulations (asterisks). The comparison shows excellent agreements between the numerical and the circuit model analysis results. Besides, it is evident that as the modulation amplitude increases, the modulation indices decreases. Moreover, since the injection current for both cases of $\varepsilon = 0.07$ and 0.14 , is taken to be the same, the relaxation oscillation frequencies are almost the same, ~ 18.5 GHz. The modulation spectra for the cross-port signals, with peaks observed around the relaxation oscillation frequencies, resemble that of the conventional FP laser whose bandwidth is limited by the relaxation oscillation frequency. As the modulation frequency increases beyond the relaxation oscillation frequency, strong damping is observed, for each case. It is because, for this frequency range, the carrier and photon dynamics are not capable of following each other. Nonetheless, the through-port power modulation bandwidth (cut-off frequency), extending to the THz frequency range (Fig. 7(a)), significantly differs from that of the cross-port.

It is worth noting that contrary to the cross-port power that has no phase dependence, a small signal fluctuation in the through-port power is related to $\Delta\phi$, the phase difference of the counter-propagating signals. As shown in [11] relaxation oscillation frequency does not limit the characteristic relaxation rate for the phase difference. Nonetheless, the total rate by which the phase coherence decays ($\gamma_L + \gamma_T$) governs the relaxation rate

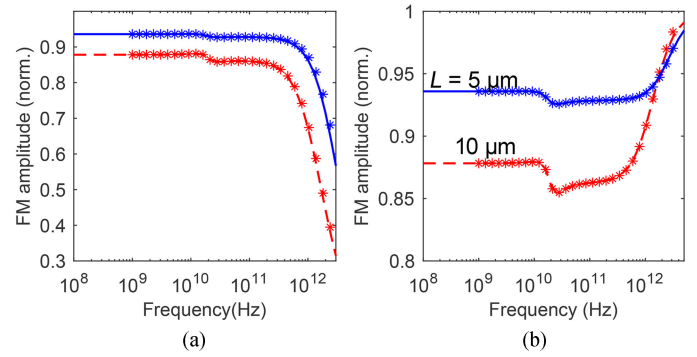


Fig. 8. The FM amplitude normalized to the maximum variation of the nanocavity resonance, $\varepsilon\gamma_T$, versus the nanocavity modulation frequency, for (a) A^+ and (b) A^- field envelopes, for $L = 5 \mu\text{m}$ (solid lines) and $10 \mu\text{m}$ (dashes), obtained by the circuit model simulations. Asterisk represents the results of numerical simulations.

for the phase difference, resulting in a THz bandwidth. This dependence extends the bandwidth of the through-port modulation index to beyond 1 THz.

Finally, we simulate the frequency dependence of the FM amplitudes of the two counter-propagating fields in two PhC-FL cavities of different lengths, using the circuit and numerical models, as illustrated in Fig. 8. The solid line and dashes in Fig. 8(a) represent the FM amplitude for A^- , obtained by the circuit model analysis for $L = 5$ and $10 \mu\text{m}$, with the same Q_T , while asterisks depict the results obtained by the numerical approach. Note that each FM amplitude response experiences the same resonance frequency as its corresponding intensity modulation observes. Because the coupling between phase and amplitude mediated by the Fano mirror is the cause of this resonance [13]. Fig. 8(a) also reveals that, for a given Q_T , as L increases (γ_L decreases) the modulation bandwidth (cut-off frequency) that depends on the inverse of the laser cavity round-trip time decreases, similar to that discussed in [11].

Fig. 8(b) shows that the FM amplitude of the propagating field envelope (A^-) in cross-port increases towards unity with the modulation frequency. This behavior reflects that the cross-port field instantaneously tracks the nanocavity field change. It is worth noting that as the modulation exceeds the intermode-spacing, the model becomes inaccurate [13]. Nonetheless, since the intermode-spacing is much greater than the relaxation oscillation resonance frequency, we may safely analyze the modulation response in the high-frequency regime. Based on these results one can conclude that small signal modulation of the Fano mirror resonance frequency has no effects on the laser power and the active region carrier density. It is because it changes the phase and frequency of the field in the nanocavity via the adiabatic wavelength conversion mechanism that is in contrast to the case of current modulation [11]. The present small signal analysis shows that the nanocavity-modulated PhC-FL does not experience the usual bandwidth limitation imposed by the relaxation oscillations that is dominant in the conventional current-modulated FP lasers [11], [25].

VI. CONCLUSION

We have proposed a new equivalent circuit model that is a cost-effective and fast tool for the design of PhC-FLs. This new model is mainly a set of six coupled linear electrical circuits. We have compared the new results obtained by solving this new set of equations via HSPICE circuit simulator with those obtained from the computationally exhaustive numerical simulation of the full set of differential equations. The comparison has shown excellent agreements between both sets of results, demonstrating that the proposed circuit model offers a fast, simple, and computationally effective approach that can best describe the PhC-FL modulation response. Moreover, using the circuit model, we have simulated the frequency response of a PhC-FL to the conventional current modulation and also to the modulation of the nanocavity resonance frequency. These simulations have shown that the Fano laser has the prospect of being modulated at frequencies of several hundred gigahertz via modulation of the nanocavity. Furthermore, the effect of the detuning on the modulation properties was thoroughly investigated, showing that this provides another possibility to increase the PhC-FL relaxation oscillation frequency. It has been also shown that the bandwidth of the modulation response can be increased by decreasing the length of the active area. The simulation results, in general, indicate that the developed small signal circuit model can be a very useful tool for simulation of the PhC-FLs.

APPENDIX

$$\begin{aligned}\tau_{11} &\equiv [\gamma_L (1 - \Gamma L g_N \Delta N)]^{-1} \equiv R_1 C_1 \\ \tau_{12} &\equiv -R_R [\gamma_L (r_{RR} \sin \Delta \phi + r_{RI} \cos \Delta \phi) a^-]^{-1} \equiv C_1 G_{12}^{-1} \\ \tau_{13} &\equiv R_R [\gamma_L (r_{RR} \cos \Delta \phi - r_{RI} \sin \Delta \phi)]^{-1} \equiv C_1 G_{13}^{-1} \\ \tau_{14} &\equiv R_R [\gamma_L (r_{RR} \sin \Delta \phi + r_{RI} \cos \Delta \phi) a^-]^{-1} \equiv C_1 G_{14}^{-1} \\ \tau_{15} &\equiv (\gamma_L \Gamma L g_N a^+)^{-1} \equiv C_1 G_{15}^{-1}\end{aligned}\quad (A1)$$

$$\begin{aligned}\tau_{21} &\equiv R_R [\gamma_L (r_{RR} \sin \Delta \phi + r_{RI} \cos \Delta \phi) a^-]^{-1} (a^+)^2 \\ &\equiv C_2 G_{21}^{-1} \\ \tau_{22} &\equiv R_R [\gamma_L (r_{RR} \cos \Delta \phi - r_{RI} \sin \Delta \phi) a^-]^{-1} a^+ \equiv C_2 R_2 \\ \tau_{23} &\equiv -R_R [\gamma_L (r_{RR} \sin \Delta \phi + r_{RI} \cos \Delta \phi)]^{-1} a^+ \equiv C_2 G_{23}^{-1} \\ \tau_{24} &\equiv R_R [\gamma_L (r_{RR} \cos \Delta \phi - r_{RI} \sin \Delta \phi) a^-]^{-1} a^+ \equiv C_2 G_{24}^{-1} \\ \tau_{25} &\equiv -[\gamma_L L \alpha \Gamma g_N]^{-1} \equiv C_2 G_{25}^{-1}\end{aligned}\quad (A2)$$

$$\begin{aligned}\tau_{31} &\equiv (\gamma_c \cos \Delta \phi)^{-1} \equiv C_3 G_{31}^{-1} \\ \tau_{32} &\equiv -(\gamma_c \sin \Delta \phi a^+)^{-1} \equiv C_3 G_{32}^{-1} \\ \tau_{33} &\equiv (\gamma_T - \gamma_L L \Gamma_c g_N \Delta N_{CA})^{-1} \equiv C_3 R_3 \\ \tau_{34} &\equiv (\gamma_c \sin \Delta \phi a^+)^{-1} \equiv C_3 G_{34}^{-1} \\ \tau_{36} &\equiv (\gamma_L L \Gamma_c g_N a^-)^{-1} \equiv C_3 G_{36}^{-1}\end{aligned}\quad (A3)$$

$$\begin{aligned}\tau_{41} &\equiv (\gamma_c \sin \Delta \phi)^{-1} a^- \equiv C_4 G_1^{-1} \\ \tau_{42} &\equiv (\gamma_c \cos \Delta \phi a^+)^{-1} a^- \equiv C_4 G_{42}^{-1} \\ \tau_{43} &\equiv -(\gamma_c \sin \Delta \phi a^+)^{-1} (a^-)^2 \equiv C_4 G_{43}^{-1} \\ \tau_{44} &\equiv (\gamma_c \cos \Delta \phi a^+)^{-1} a^- \equiv C_4 R_4 \\ \tau_{46} &\equiv -(\gamma_L L \alpha \Gamma_c)^{-1} \equiv C_4 G_{46}^{-1}\end{aligned}\quad (A4)$$

$$\begin{aligned}\tau_{51} &\equiv -V_m (4\gamma_L L \sigma g_N \Delta N' a^+)^{-1} \equiv C_5 G_{51}^{-1} \\ \tau_{55} &\equiv \left(2\gamma_L L g_N \frac{I_p}{V_m} + \frac{1}{\tau} \right)^{-1} \equiv C_5 R_5\end{aligned}\quad (A5)$$

$$\begin{aligned}\tau_{63} &\equiv -V_{CA} (4\gamma_L L \rho \Gamma_c g_N \Delta N_{CA} a^-)^{-1} \equiv C_6 G_{63}^{-1} \\ \tau_{66} &\equiv \left(2\gamma_L L \rho \Gamma_c g_N (a^-)^2 V_{CA}^{-1} + \frac{1}{\tau} \right)^{-1} \equiv C_6 R_6\end{aligned}\quad (A6)$$

where $r_{RR} = \text{Re}(r_R)$ and $r_{RI} = \text{Im}(r_R)$ are the real and imaginary parts of the Fano mirror reflectance, $R_R = |r_R(\omega_s, \omega_c)|^2$, and $\Delta \phi = \phi^+ - \phi^-$.

REFERENCES

- [1] O. Painter *et al.*, "Two-dimensional photonic band-gap defect mode laser," *Science*, vol. 284, no. 5421, pp. 1819–1821, 1999.
- [2] H.-G. Park *et al.*, "Electrically driven single-cell photonic crystal laser," *Science*, vol. 305, no. 5689, pp. 1444–1447, 2004.
- [3] T. Baba *et al.*, "Observation of fast spontaneous emission decay in GaInAsP photonic crystal point defect nanocavity at room temperature," *Appl. Phys. Lett.*, vol. 85, no. 18, pp. 3989–3991, 2004.
- [4] H. Altug, D. Englund, and J. Vučković, "Ultrafast photonic crystal nanocavity laser," *Nature Phys.*, vol. 2, no. 7, pp. 484–488, 2006.
- [5] D. Englund, H. Altug, B. Ellis, and J. Vučković, "Ultrafast photonic crystal lasers," *Laser Photon. Rev.*, vol. 2, no. 4, pp. 264–274, 2008.
- [6] S. Matsuo *et al.*, "High-speed ultracompact buried heterostructure photonic-crystal laser with 13 fJ of energy consumed per bit transmitted," *Nature Photon.*, vol. 4, pp. 648–654, 2010.
- [7] S. Matsuo *et al.*, "Ultralow operating energy electrically driven photonic crystal lasers," *IEEE J. Sel. Topics Quantum Electron.*, vol. 19, no. 4, Jul./Aug. 2013, Art. no. 4900311.
- [8] W. Xue *et al.*, "Threshold characteristics of slow-light photonic crystal lasers," *Phys. Rev. Lett.*, vol. 116, no. 6, 2016, Art. no. 063901.
- [9] K. Kiyota, T. Kise, N. Yokouchi, T. Ide, and T. Baba, "Various low group velocity effects in photonic crystal line defect waveguides and their demonstration by laser oscillation," *Appl. Phys. Lett.*, vol. 88, no. 20, 2006, Art. no. 201904.
- [10] Y. Zhang *et al.*, "Photonic crystal nanobeam lasers," *Appl. Phys. Lett.*, vol. 97, no. 5, 2010, Art. no. 051104.
- [11] J. Mork, Y. Chen, and M. Heuck, "Photonic crystal fano laser: Terahertz modulation and ultrashort pulse generation," *Phys. Rev. Lett.*, vol. 113, no. 16, 2014, Art. no. 163901.
- [12] T. S. Rasmussen, Y. Yu, and J. Mork, "Theory of Self-pulsing in photonic crystal fano lasers," *Laser Photon. Rev.*, vol. 11, no. 5, 2017, Art. no. 1700089.
- [13] T. S. Rasmussen, Y. Yu, and J. Mork, "Modes, stability, and small-signal response of photonic crystal fano lasers," *Opt. Express*, vol. 26, no. 13, pp. 16365–16376, 2018.
- [14] Y. Yu, W. Xue, E. Semenova, K. Yvind, and J. Mork, "Demonstration of a self-pulsing photonic crystal fano laser," *Nature Photon.*, vol. 11, no. 2, pp. 81–84, 2017.
- [15] A. R. Zali, M. K. Moravvej-Farshi, Y. Yu, and J. Mork, "Small and large signal analysis of photonic crystal fano laser," *J. Lightw. Technol.*, vol. 36, no. 23, pp. 5611–5616, Dec. 2018.
- [16] S. Fan, "Sharp asymmetric line shapes in side-coupled waveguide-cavity systems," *Appl. Phys. Lett.*, vol. 80, no. 6, pp. 908–910, 2002.
- [17] Y. Yu *et al.*, "Nonreciprocal transmission in a nonlinear photonic-crystal Fano structure with broken symmetry," *Laser Photon. Rev.*, vol. 9, no. 2, pp. 241–247, 2015.

- [18] E. Mortazy, V. Ahmadi, and M. K. Moravvej-Farshi, "An integrated equivalent circuit model for relative intensity noise and frequency noise spectrum of a multimode semiconductor laser," *IEEE J. Quantum Electron.*, vol. 38, no. 10, pp. 1366–1371, Oct. 2002.
- [19] P. V. Mena, S.-M. Kang, and T. A. DeTemple, "Rate-equation-based laser models with a single solution regime," *J. Lightw. Technol.*, vol. 15, no. 4, pp. 717–730, Apr. 1997.
- [20] P. V. Mena, *Circuit-Level Modeling and Simulation of Semiconductor Lasers*. Champaign, IL, USA: Univ. Illinois Urbana-Champaign, 1998.
- [21] T. T. Bich-Ha and J.-C. Mollier, "Noise equivalent circuit of a two-mode semiconductor laser with the contribution of both the linear and the nonlinear gain," *IEEE J. Sel. Topics Quantum Electron.*, vol. 3, no. 2, pp. 304–308, Apr. 1997.
- [22] M. H. Yavari and V. Ahmadi, "Circuit-level implementation of semiconductor self-assembled quantum dot laser," *IEEE J. Sel. Topics Quantum Electron.*, vol. 15, no. 3, pp. 774–779, May/Jun. 2009.
- [23] J. D. Joannopoulos, S. G. Johnson, J. N. Winn, and R. D. Meade, *Photonic Crystals: Molding the Flow of Light*. Princeton, NJ, USA: Princeton Univ. Press, 2011.
- [24] Y. Yu *et al.*, "Switching characteristics of an InP photonic crystal nanocavity: experiment and theory," *Opt. Express*, vol. 21, no. 25, pp. 31047–31061, 2013.
- [25] L. A. Coldren, S. W. Corzine, and M. L. Mashanovitch, *Diode Lasers and Photonic Integrated Circuits*. Hoboken, NJ, USA: Wiley, 2012.
- [26] A. F. Koenderink, M. Kafesaki, B. C. Buchler, and V. Sandoghdar, "Controlling the resonance of a photonic crystal microcavity by a near-field probe," *Phys. Rev. Lett.*, vol. 95, no. 15, 2005, Art. no. 153904.
- [27] L.-D. Haret *et al.*, "Schottky MSM junctions for carrier depletion in silicon photonic crystal microcavities," *Opt. Express*, vol. 21, no. 8, pp. 10324–10334, 2013.
- [28] M. Heuck, P. T. Kristensen, Y. Elesin, and J. Mørk, "Improved switching using Fano resonances in photonic crystal structures," *Opt. Lett.*, vol. 38, no. 14, pp. 2466–2468, 2013.

Aref Rasoulzadeh Zali was born in Tabriz, Iran, in 1986. He received the B.Sc. degree from Tabriz University, Tabriz, in 2010, and the M.A. degree from Tarbiat Modares University, Tehran, Iran, in 2012, both in electrical engineering. He joined as a Visiting Researcher to Prof. Jesper Mørk's group at Technical University of Denmark (DTU), in 2016. His research interests include photonic devices such as photodetectors, lasers, and SOAs.

Mohammad Kazem Moravvej-Farshi (SM'05) was born in Yazd, Iran, in 1952. He received the B.Sc. degree from the Sharif University of Technology, Tehran, Iran, in 1976, the M.A. degree from the University of Southern California, Los Angeles, CA, USA, in 1978, both in physics, and the M.Sc. degree from the University of California at Santa Barbara, Santa Barbara, CA, USA, in 1980, and the Ph.D. degree from the University of New South Wales, Sydney, NSW, Australia, in 1987, both in electronics. From 1980 to 1984, he was a member of research staff with the Division of Microwave, Iran Telecommunication Research Center (ITRC). He joined Tarbiat Modares University in 1987, where he is currently a Professor of Electronics and Head of the Nano Plasm-Photonic Research Group. Prof. Moravvej-Farshi is currently a senior member of the Optical Society of America (OSA). He is also one of the founders of the Optics and Photonics Society of Iran, where he has been the Chairman of the board of directors, since November 2016.

Mohammad Hassan Yavari (S'02–M'10) was born in Yazd, Iran, in 1978. He received the M.Sc. and Ph.D. degrees in electronic engineering from Tarbiat Modares University, Tehran, Iran, in 2004 and 2010, respectively. His Ph.D. dissertation focused on the numerical modeling and analysis of self-assembled quantum dot lasers. He was a Visiting Researcher in Prof. Bimberg's group at the Technical University of Berlin, Germany, in 2011. He is currently with the Department of Electronic Engineering, Shahed University, Tehran. His research interests include the areas of nano photonic devices specializing in the field of semiconductor lasers and amplifiers.